

In-situ

3D printing of diamond-coated carbon fiber reinforced polymer (CFRP) composites



Changchun Li^a, Wuxi Xie^a, Lili Zhang^{a,*}, Liang He^b, Changchun Li^c, Lili Zhang^d,
Wuxi Xie^e, Kewei Li^f, Lili Zhang^g, Xing Gao^h, Tian Pengⁱ

^a Gemmological Institute, China University of Geosciences, Wuhan 430074, PR China
^b Hubei Gem and Jewelry Engineering Technology Research Center, Wuhan 430074, PR China
^c School of Materials Science and Engineering, Huazhong University of Science and Technology, Wuhan 430074, PR China
^d Mechanical Engineering, University of Birmingham, Birmingham B15 2TT, UK
^e School of Electrical and Electronic Engineering, Huazhong University of Science and Technology, Wuhan 430074, PR China
^f WMG, Materials Engineering Centre, University of Warwick, CV4 7AL Coventry, UK

ARTICLE INFO

Keywords:

3D printing
Carbon fiber
SLM
CVD
EMI

ABSTRACT

Carbon fiber reinforced polymer (CFRP) composites are widely used in aerospace, automotive, and other industries. However, the traditional manufacturing process of CFRP composites is time-consuming and expensive. In this paper, a 3D printing method is proposed to fabricate CFRP composites. The CFRP composites are fabricated by selective laser melting (SLM) of a carbon fiber reinforced polymer (CFRP) powder. The CFRP composites are coated with diamond (CVD) by chemical vapor deposition (CVD). The CFRP composites are tested for mechanical properties and electromagnetic interference (EMI) shielding. The CFRP composites show a tensile strength of 47.8 MPa and a tensile modulus of 2.7 GPa. The CFRP composites show an EMI shielding effectiveness (SE) of 32.3 dB in the frequency range of 2–18 GHz. The CFRP composites show a high EMI shielding effectiveness (SE) of 32.3 dB in the frequency range of 2–18 GHz. The CFRP composites show a high EMI shielding effectiveness (SE) of 32.3 dB in the frequency range of 2–18 GHz.

1. Introduction

Graphene (sp^2 carbon) is a two-dimensional material with a hexagonal lattice structure. It has a high tensile strength of 2630 N m⁻¹ [1], a high thermal conductivity of 5000 W m⁻¹ K⁻¹ [2], and a high electrical conductivity of 3.1 × 10⁸ S m⁻¹ [3]. A large number of studies have shown that graphene has a wide range of applications in various fields, such as energy storage, catalysis, and electronics [4].

(2DG), 5, 6, 7, 8, 9, 10, 11, 12, 13, 14, 15, 16. B

*Corresponding author. E-mail address: llzhang@cug.edu.cn (L. Zhang).

. T (2., fi
) , fl fi
(.,) 3DG. B
3DG w
(.,). H w
ffi
N
3DG w
fi 17,18
H , w
3DG w
19
S (SLM),
(AM)
(3D)
w ffi
fl *in-situ* T
SLM T 20
21 , N 22 . C w
C w N
w
CVD w (< 0.001 .%)
w , w
23 . W N
(> 0.1 .%) 17 , fi
24 . H w
SLM ffi
w
fl w w
(1000–1100). F ff
SLM 25
T , w fi
3DG/ (3DG/C)
SLM w CVD w
A w
SLM

T , TJ/T112T 0.8.0160T (2 /T101T 0.982575T ()-33428(w)-44516()-41120())-334.62
-579684 :574TD(3D7(574((> 32(5748(103JT9207740 5159-11.0 1228302(50T (7 00.4.70TD 770320 7703218(8(097.6787T (S

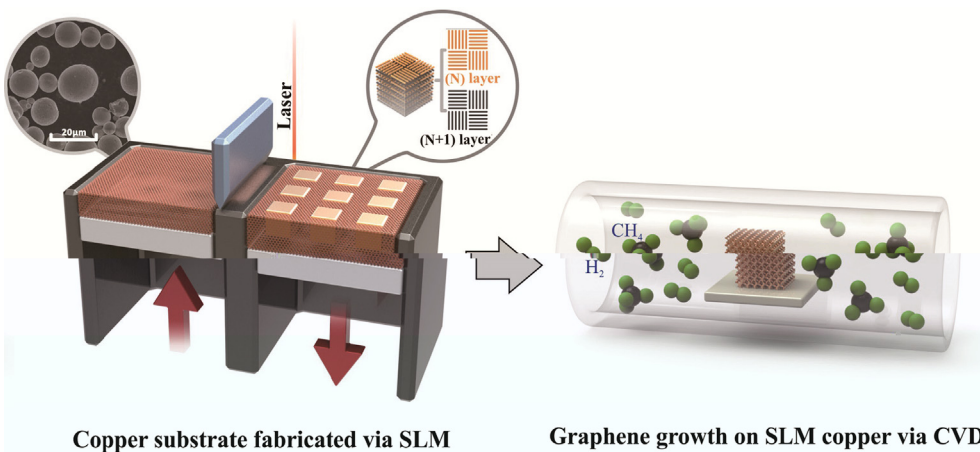


Fig. 1. (a) Schematic of SLM process for copper substrate fabrication. (b) Schematic of CVD process for graphene growth on SLM copper substrate. (c) SEM image of SLM copper substrate showing a porous structure with a magnified view of the powder particles (20µm). (d) SEM image of graphene grown on SLM copper substrate showing a porous structure with a magnified view of the graphene layers (N layer and N+1 layer).

ASTMB193-2002
 (5 10 10³)
 N LFA457, G
 G
 514
 US)
 S

SLM ()
 in-situ
 (F L 2)
 30% w
 (A), 26.7%
 (B), 16.7%
 (C) 26.7%
 (D). D
 LED (J/) 27 (E . 6,
 SI). T
 LED 400 J/ (C). W
 (> 800 J/)
 130 µ
 (D), w
 28 .

3. Results and discussion

3.1. Formation of SLM copper

3.1.1. SLM manufacturing of copper under different line energy densities

T ff (w)
 w D ff

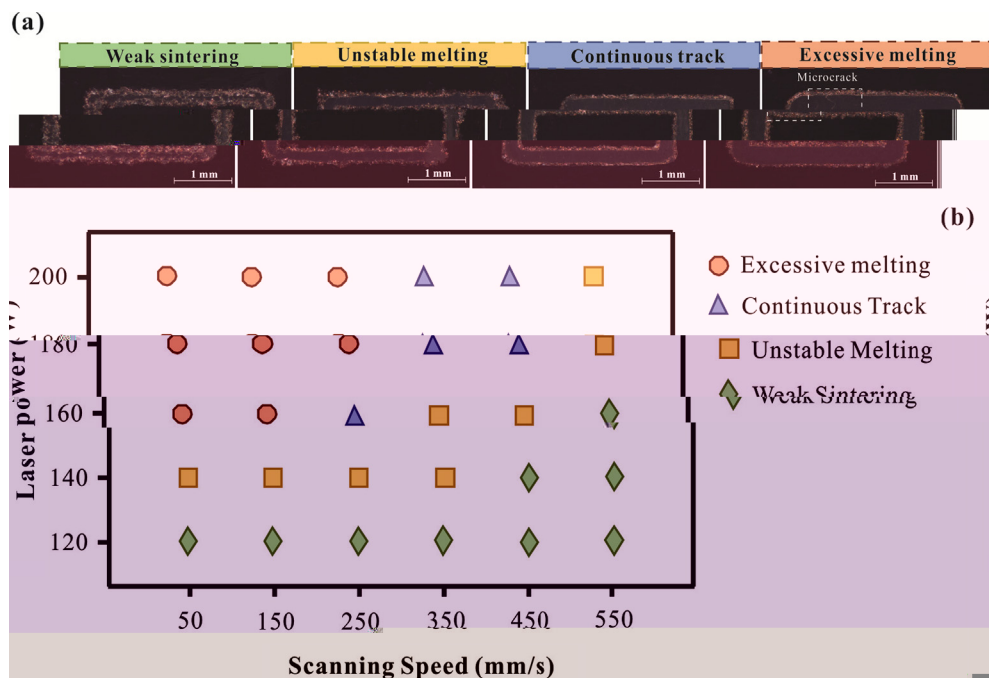


Fig. 2. (a) SEM images of SLM copper tracks under different conditions: Weak sintering, Unstable melting, Continuous track, and Excessive melting. (b) Scatter plot of Laser power (W) vs Scanning Speed (mm/s) for different conditions.

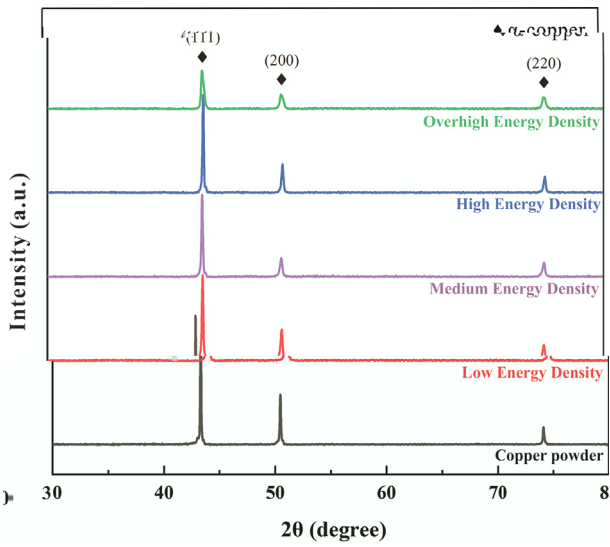


Fig. 3. XRD patterns of copper powder at different energy densities.

3.1.2. Formation of anisotropic microstructure under different volumetric energy density

The XRD patterns of copper powder at different energy densities are shown in Fig. 3. The peaks are indexed to the (111), (200), and (220) planes of copper. The peak positions are $2\theta = 43.32^\circ$, 50.45° , and 73.52° , respectively (Fig. 3). The intensity of the (111) peak is significantly higher than that of the (200) and (220) peaks, indicating a strong preferential orientation of the (111) plane. The intensity of the (111) peak increases with increasing energy density, while the intensity of the (200) and (220) peaks decreases. This indicates that the (111) plane is the dominant orientation of the copper powder at different energy densities.

The microstructures of the copper powder at different energy densities are shown in Fig. 4. The microstructures are characterized by the presence of voids and inter-layer voids. The voids are formed during the SLM process due to the evaporation of the powder particles. The inter-layer voids are formed due to the incomplete fusion of the powder particles. The microstructures show that the voids and inter-layer voids increase with increasing energy density. This is due to the fact that the higher energy density leads to a higher temperature, which causes the powder particles to evaporate more readily and to fuse less completely. The microstructures also show that the voids and inter-layer voids are more numerous and larger in size at higher energy densities. This is due to the fact that the higher energy density leads to a higher temperature, which causes the powder particles to evaporate more readily and to fuse less completely. The microstructures show that the voids and inter-layer voids increase with increasing energy density. This is due to the fact that the higher energy density leads to a higher temperature, which causes the powder particles to evaporate more readily and to fuse less completely. The microstructures also show that the voids and inter-layer voids are more numerous and larger in size at higher energy densities. This is due to the fact that the higher energy density leads to a higher temperature, which causes the powder particles to evaporate more readily and to fuse less completely.

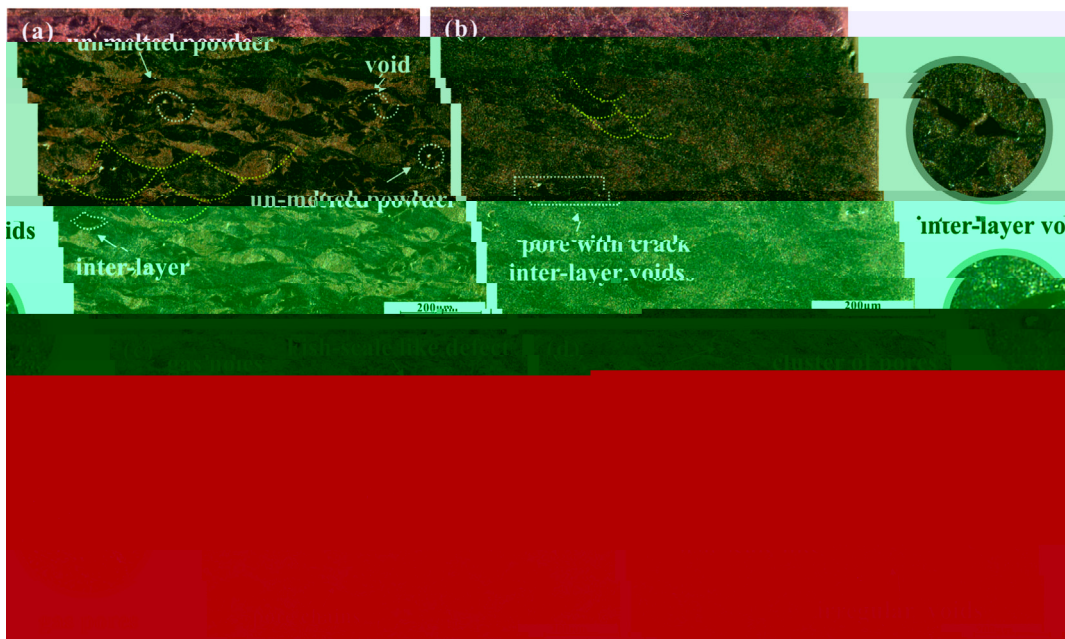


Fig. 4. SEM images of copper powder at different energy densities: (a) (3000 J/mm³), (b) (857 J/mm³), (c) (285 J/mm³), (d) (128 J/mm³), (e) (180 J/mm³). (Figs. 4a-e).

... ..

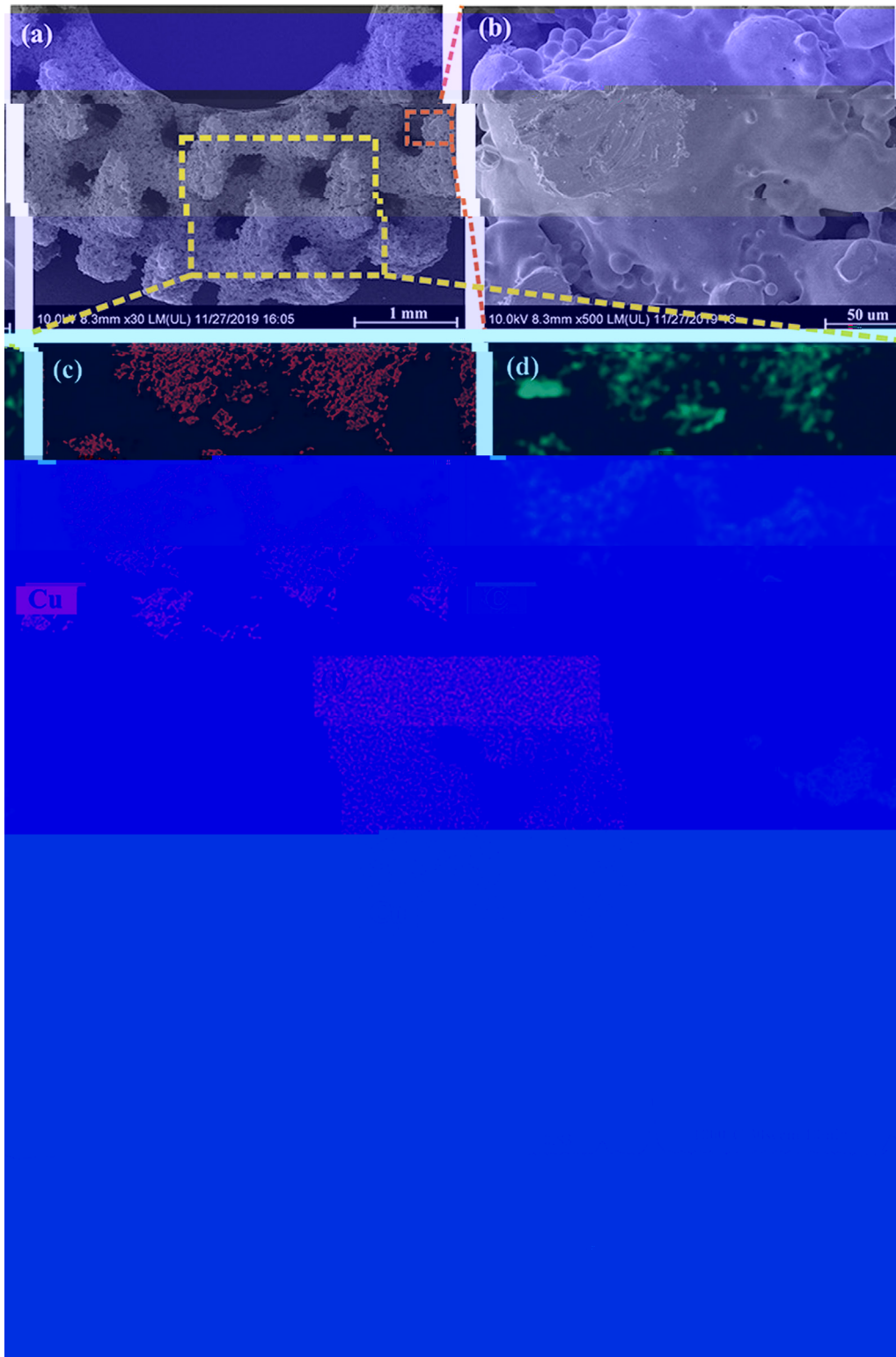


Fig. 8. (a) SEM image of 3DG/Cu porous scaffold; (b) SEM image of porous structure; (c) EDS elemental map of C; (d) EDS elemental map of Cu. The inset is the EDS spectrum of the porous scaffold.

...W...
 I_D/I_G ... 0.71 ... 0.93, ...
 ...A...
 ...1000 C, fl w ...
 ...20 ... w ...
 ...3DG/C

3.4. Thermal property and EMI shielding effectiveness of 3DG/Cu porous scaffolds

T ... ff ...
 ...C ...
 ...26.8% ...
 ...14.8% ...

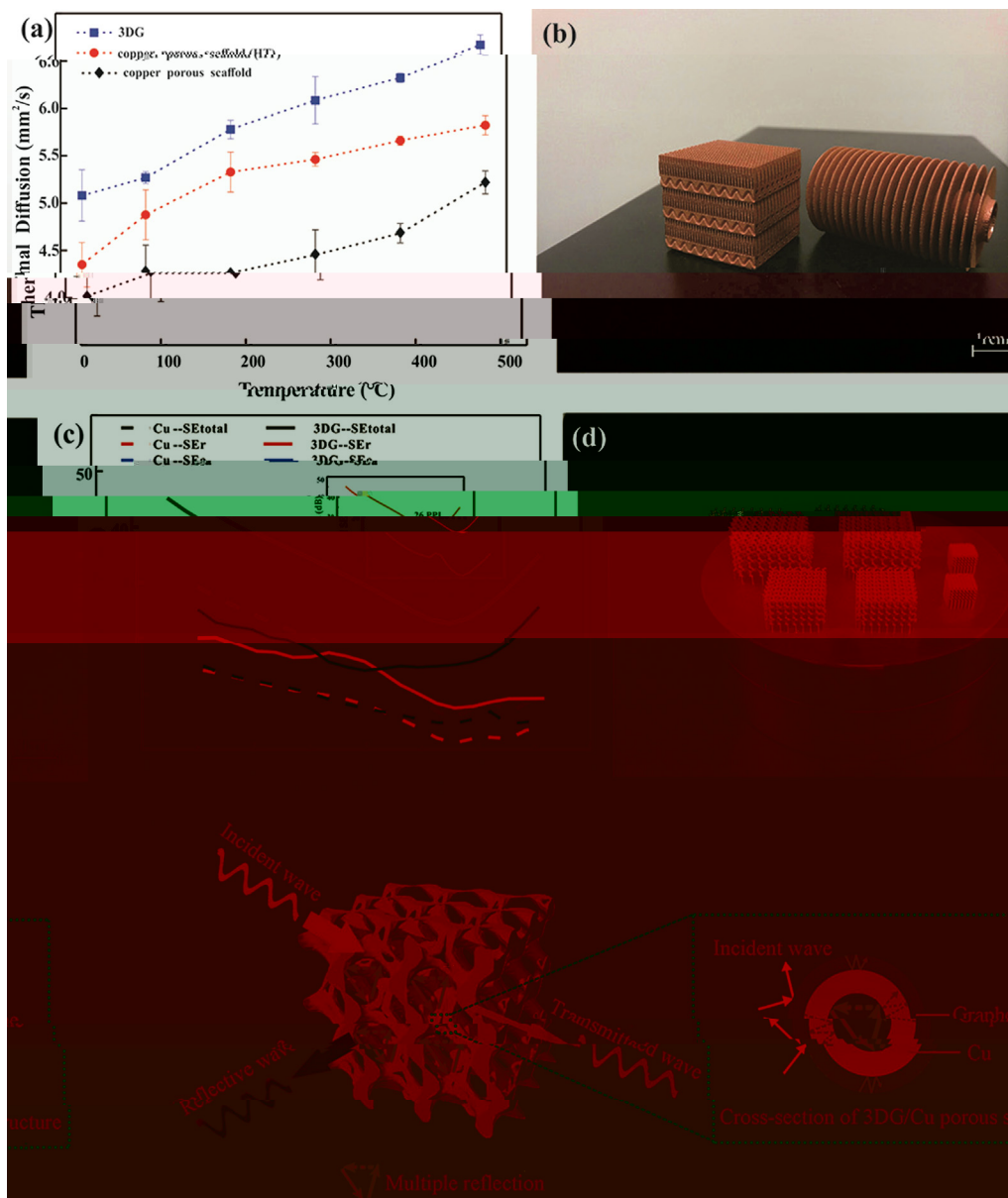


Fig. 9. (a) Thermal Diffusion of 3DG/Cu porous scaffold (□) and copper porous scaffold (○) SLM fabricated porous scaffold (HT) (●) (b) 3D models of 3DG and copper porous scaffold. (c) SEM images of Cu-SEtotal, Cu-SEr, Cu-SEa, 3DG-SEtotal, 3DG-SEr, and 3DG-SEa. (d) Schematic of wave propagation through the 3DG/Cu porous scaffold structure.

Table 1

Comparison of the maximum shielding efficiency (SE) and improvement of thermal property (%) of various porous scaffolds. (□) PPMA, (○) PS.

Coating materials	Substrate	Method	Maximum shielding efficiency (dB)	Improvement of thermal property (%)	Ref
G...	G...	I...	37	-	50
G...	PS	H...	29.3	-	56
G...	PMMA	S...	19	-	57
C/G...	A...	S...	-	8.5	58
G...	N...	F...	-	554	59
G...	C-N...	E...	20	-	60
G...	C	P w...	-	2.4	61
G...	C	F...	47	6.3	62
G...	C	CVD + SLM	47.8	27	T...

Note: (□) PPMA, (○) PS.

HT
in-situ w (F. 9a). S
 3DG/C ff
 HT
 1-2
 W
 SLM
 fl w (w fl) 500 μm
 (F. 9b),
 G
 (T. 1). I
 O
 T
 EMI, EMI SE, w 3DG/C ff
 (EM) w
 2-18 GHz (F. 9c),
 W *in-situ* w
 ff SE 15.9 32.3 B, w
 47.8 B (88.2%),
 20 B. T
 3DG/C fi
 J K 44 EMI
 w T EMI SE
 133%) 20 110 PPI ().
 R K 45 EMI
 W
 17 26 PPI (F. 9c insert) 105%
 EMI SE. I w EMI
 ff w SLM. T
 3DG/C 26 PPI EMI SE
 32.3 B, 99.9% EMI w T
 60
 (30 ff) 46 T EMI
 3DG/C w
 T 1. I EMI SE
 3DG/C w
 3D
 T EMI fl (SE_r),
 (SE_a) fl (EM) w 47,
 w
 48 R 49 w
 w, w
 T w EM w
 fi
 50 R EMI
 T
 w w w
 w fi C 51 F
 w
 52 S O₂ 53 W
 3DG/C ff w

SE_r, SE_a, w F. 9e. W w
 w 3DG/C ff
 w w fl w ff S
 3DG/C
 fi
 w w T
 EM w fi w w
 w EM w
 SE_r, O
 w ff, w w fi EM
 w ff EM
 T
 ff w
 w J 54 I w
 fi w
 fl ff M
 w
 w fi
 EM w
 EM w T
 w 44 T
 w 3D EM w w
 I CVD
 R S 3.3
 55 I
 EM w w O w
 3DG/C
 fi w fi
 T
 w ff

4. Conclusions

A 3DG/C ff w w
in-situ CVD w
 T ff W 3DG/C
 EMI SE
 15.9 () 32.3 B,
 47.8 B (88.2%), w 26.8%
 ff T 3DG/C
 ff fl fi
 T EMI
 3DG/C ff
 EMI

Credit authorship contribution statement

Kaka Cheng: C, M, F, W
 Wei Xiong: V, I, W
 Yan Li: W &, F
 Liang Hao: F, Chunze Yan: R, F
 Zhaoqing Li: V, Zhufeng Liu: F
 Yushen Wang: I, S, Khamis Essa: W &
 Li Lee: D, Xin Gong: S
 Ton Peijs: W &, S

Declaration of Competing Interest

T... fl...

Acknowledgement

T... w... fi... N... N... S... F... C... (N... 51671091, N... 51902295, N... 51675496). T... F... R... F... C... U... C... U... G... (W...) (N... CUG170677), H... P... N... S... F... (N... 2019 CFB264).

Appendix A. Supplementary data

S... // /10.1016/... .2020.105904.

References

1 B... RG, N... N, M... K, M... S. G... ACS N... 2018;91:24-69.

2 B... AA, G... S, B... W, C... L, T... D, M... F, S... ACS N... 2008;8(3):902-7.

3 L... H, C... M, P... w, H... P, O... S, G... ACS A... M... 2016;8(36):24112-22.

4 K... M, K... J, J... B, C... K, J... H, A... J... H... G... ACS N... 2017;11(8):7950-7.

5 P... C... M, H... M, T... M, L... D, P... ACS N... 2020;262:118266-76.

6 L... XJ, W... C, LL, J... SH, W... G, L... F... C-G... ACS N... 2017;101:50-8.

7 H... Q, L... SW, C... LH, J... SH, H... HQ, S... ACS N... 2018;6(42):21216-24.

8 D... TM, S... P, D... P, K... J, Kw... M, A... T, ACS N... 2017;1(4):467-70.

9 Q... L, L... L, T... ACS A... 2014;4(72):38273-80.

10 D... X, H... L, SP, N... W, J... G. 3D... ACS N... 2016;90:424-32.

11 L... XL, X... W, S... CQ, H... MK, X... HL, D... W, ACS N... 2018;100:201803938.

12 L... J, P... X, C... R, G... N... D... G... ACS N... 2013;7(7):6001-6.

13 J... SH, A... w, S... G... A... L... ACS N... 2017;56:15520-38.

14 I... T... S... w... K, K... M, T... T, T... K... ACS N... 2018;20(9):6024-33.

15 S... K, D... N, M... C, V... N, E... J... T... ACS N... 2002;149(8):370-7.

16 C... XH, S... M, S... WH, L... G, H... X... Q... ACS N... 2011;7(22):3163-8.

17 K... H, G... M, J... I, H... J, W... C, C... M... ACS N... 2019;1(4):1077-87.

18 S... Q, F... X, L... W, L... H... ACS N... 2017;29(31):1701583-90.

19 X... X, G... C, X... L, T... H... D, W... ACS N... 2019;101:101908191.

20 C... C, H... B... X, N... J, C... S, L... F... ACS N... 2019;175:107824-33.

21 S... Š... J, B... Ž... D... T... ACS N... 2016;307:407-17.

22 R... DC, HB, L... J, L... SJ, J... W, ACS N... 2020;771:138586-95.

23 L... X, C... W, A... J, K... S, N... J... ACS N... 2009;324(5932):1312-4.

24 C... P, R... WC, G... LB, L... BL, P... SE, C... HM. T... ACS N... 2011;10:424-8.

25 J... SD, D... S, G... L, K... JP, H... JV, V... ACS N... 2019;270:47-58.

26 X... W, H... L, L... T... D, C... Q, F... ACS N... 2019;170:107697-708.

27 G... DD, M... W, W... K, P... ACS N... 2013;57(3):133-64.

28 L... E, T... S, C... L, F... ACS N... 2017;249:255-63.

29 X... S, W... L, J, W... P, C... ACS N... 2018;124:685-98.

30 L... M... S, D... W, S... C... ACS N... 2015;87:797-806.

31 L... CLA, M... S, T... w... M, A... w... ACS N... 2019;166:294-305.

32 T... X, K... T... WQ, T... J, D... M, M... D, ACS N... 2016;6:26039-48.

33 K... H, T... XP, L... NH, T... SB, C... CK. G... ACS N... 2016;11(3):183-91.

34 R... fi HK, K... NV, G... H, S... TL, S... ACS N... 2013;22(12):3872-83.

35 T... X, K... T... J, V... G, P... QX, ACS N... 2015;646:303-9.

36 R... DA, M... LE, M... H... ACS N... 2011;59(10):4088-99.

37 X... W... H... ACS N... 2018;743:258-61.

38 K... S... W... ACS N... 2003;23:309-48.

39 L... G... G... J... ff... R... G... ACS N... 2010;10(9):3512-6.

40 L... XS, C... WW, C... L... R... ACS N... 2009;9(12):4268-72.

41 X... W, X... C... X... W... H... ACS N... 2020;161:479-85.

42 F... AC, M... JC, S... V... C... ACS N... 2006;97(18):187401-4.

43 S... G... J... SH, F... PC, H... HQ. F... ACS N... 2017;200:97-100.

44 J... K... H... J... C... J... D... ACS N... 2014;311:351-6.

45 R... K... M... DP, A... C... M... S... S... ACS N... 2018;12:475-84.

46 S... B... L... W... W... C... ACS N... 2016;8(12):8050-7.

M 2019;34(5):489–98.

53 W B, C M, L M. R. *Composites Part A* 2014;26:3484–9.

54 C H, W S, J J, X C, J S. *Composites Part A* 2019;121:139–48.

55 W L, J Q, T ff MWCNT. *Composites Part A* 2015;26(3):1895–9.

56 D X, P GR, H P, Q F, M B, ML. *Efficient* 2012;22:18772–4.

57 HB, Q, WG, H X, T. *ACS Applied Materials* 2011;3:918–24.

58 S A, U N, T V. T. *Composites Part A* 2016. [:// doi.org/10.1051/compta/2016021](https://doi.org/10.1051/compta/2016021).

59 P MT, J H, R ff RS, S L. T. *Composites Part A* 2012;12:2959–64.

60 J K, H, H, D P. *Composites Part A* 2017;122:244–7.

61 R H, L S, B S, K TW, L DS, L HJ, T. *Composites Part A* 2015. [:// doi.org/10.1038/nmat12710](https://doi.org/10.1038/nmat12710).

62 XT, F SG, L G, Q, L G, R KP, S. *Composites Part A* 2020. [:// doi.org/10.1016/j.compositesa.2019.105670](https://doi.org/10.1016/j.compositesa.2019.105670).

63 R DA, M LE, M E, H DH, M JL, M BI, N. *Composites Part A* 2011;59(10):4088–99.

64 E SF, L KG, S VK, M IC. T. *Composites Part A* 1973;1(1):10–38.